Role of Cu–Containing MEA Binder and Sintering Temperatures on Synthesis and Characteristics of Tungsten–Based Alloys

Metals and Materials International

Aims and scope →

Submit manuscript →

Chun–Liang Chen ✉ & Sutrisna

Access this article

Role of Cu-Containing MEA Binder and Sintering Temperatures on Synthesis and Characteristics of Tungsten-Based Alloys

Chun-Liang Chen[1] · Sutrisna[1,2]

Abstract

Tungsten-based alloys doped with the 10 wt% FeCoNiCu medium entropy alloy (MEA) binder were fabricated by mechanical alloying. The role of the Cu-containing MEA binder and sintering temperatures (1250–1450°C) on the synthesis, sintering behavior, and mechanical properties of the model tungsten alloys were investigated. The results demonstrate that the solid-to-liquid phase transition during sintering was strongly influenced by the presence of Cu in the binder and sintering temperatures. A good combination of high compressive strength (2080 MPa), failure strain (42%), and hardness (419 HV) was achieved at the low sintering temperature (1250 °C), which promoted a fined grain structure with semisolid state sintering. However, Fe-rich oxide layers were formed along the grain boundaries at the high sintering temperature (1450 °C) and caused a poor bonding strength between the binder phase and W matrix, thereby resulting in significant degradation of mechanical properties.

Keywords High entropy alloy · Tungsten alloy · Mechanical alloying · Sintering behavior

1 Introduction

Tungsten heavy alloys (WHAs) are two-phase mixture materials consisting of brittle tungsten grains embedded in a ductile binder phase. WHAs have high density, high hardness, high absorption of radiation, and good wear resistance [1–3]. Therefore, they are widely used in many industrial applications such as radiation shields, kinetic energy penetrators, counterweight balance, and vibration damping devices [4, 5]. WHAs have been progressively developed by mechanical alloying over the past decades. The presence of molybdenum can enhance the hardness, yield strength, and ultimate tensile strength of tungsten heavy alloys by solid solution strengthening [6–8]. In earlier works [8], it has been also proposed that the additions of Mo and nano-oxide particles are critical to the characteristics and sintering behavior of W-Mo-Ni–Fe-Co alloys.

Transition elements of nickel, iron, cobalt, chromium, and copper are commonly utilized as a binder phase to tungsten heavy alloys for improving the strength, ductility, and toughness of materials [9–11]. Thereby, it is important to choose an appropriate binder phase for the development of new WHAs. A series of binder phases have been studied based on transition metals, which involve Ni–Fe, Ni–Fe-Co, Ni–Fe-Cu, and Ni–Fe-Cr alloy systems. [3, 12, 13].

In recent years, high entropy alloys (HEAs) have attracted considerable attention due to their excellent properties such as high strength, high ductility, and good resistance to wear, oxidation, and corrosion [14, 15]. Therefore, the use of high entropy alloys that serves as a binder phase is a promising new route in the innovation of WHAs to achieve desired performance characteristics [16–19]. It has been reported that tungsten matrix composite reinforced with CoCrFeMnNi HEA binder by spark plasma sintering exhibits higher compressive strength (~ 2041 MPa) [17]. Moreover, tungsten heavy alloy prepared using FeNiCoCrCu HEA as binder demonstrates that high compressive strength of 1912 MPa was achieved in hydrogen treated W-HEA powder sintered at 1500 °C [19].

In recent studies, the design of the binder phase based on NiFeCoCr medium entropy alloy (MEA) has been applied for tungsten heavy alloys produced by mechanical alloying

✉ Chun-Liang Chen
chunliang@gms.ndhu.edu.tw

[1] Department of Materials Science and Engineering, National Dong Hwa University, No. 1, Sec. 2, Da Hsueh Rd, Shoufeng, Hualien 97401, Taiwan

[2] Department of Mechanical Engineering, Institut Teknologi Nasional, Yogyakarta 55281, Indonesia

[18]. However, the findings indicate that a great number of Cr-rich oxides were formed in the tungsten heavy alloys after high-temperature sintering, which can deteriorate the mechanical properties of the materials. [18]. Therefore, in the present study, a new MEA binder phase of FeCoNiCu has been developed in order to prevent the effect of oxidation and improve the material's ductility. It has been reported that equimolar FeCoNiCu MEA exhibits a single FCC solid-solution phase, which has high tensile strength and good ductility [20, 21]. Furthermore, the presence of the Cu element in FeCoNiCu MEA plays an important role in determining the ductility and corrosion resistance of materials. The addition of Cu in tungsten alloys can significantly decrease the liquidus temperature and influences the sintering behavior, which further enhances the material's densification [22].

Therefore, the present research goal is to explore the contribution of the FeCoNiCu MEA binder phase and the effect of different sintering temperatures on microstructure evolution, mechanical properties, and sintering behavior of the model WHAs. Besides. it should be clarified that the role of Cu in the MEA binder phase and its interaction with the tungsten-based matrix during the mechanical alloying and sintering process. It is helpful to develop desired tungsten heavy alloys.

2 Materials and Methods

The raw materials used in this study were W, Mo, Ni, Fe, Co, and Cu elemental powders. The raw powders were purchased from a commercial supplier and have a nearly spherical morphology produced by a gas atomization process. Particle size, purity level and supplier of the raw materials are given in Table 1. The repeated fracturing and cold welding of powders during high-energy ball milling can lead to the change of the powder morphology from rounded to irregular or angular shapes. In this study, the model WHAs with the FeCoNiCu MEA binder phase were prepared by a secondary ball milling method. The W-Mo element powders were pre-milled for 8 h as a matrix phase and the 16 h of pre-milling of the FeCoNiCu MEA powders acts as a binder phase. The two phases were then further secondarily milled for 4, 8, 12, and

20 h. The chemical composition and sintering temperatures of the model WHA are listed in Table 2. Mechanical alloying was performed on a planetary ball mill (Retsch PM100) using a ball-to-powder weight ratio of 10:1 at a speed of 300 rpm under an argon atmosphere. Tungsten carbide was used as a vial and grinding media. The mechanically alloyed powders were consolidated into green compacts with ~65% of density by a pressure of 210 MPa. The green samples in the shape of cylinders (diameter of 5 mm and height of 5 ~ 7 mm) were received after the consolidation process.

The compacted powders were further sintered at various temperatures of 1250, 1350, and 1450 °C for 1 h under a mixed atmosphere consisting of 10% of hydrogen and 90% of argon. The heating rate of 2 °C/min was used as the sintering temperature increased from 950 to 1450 °C. An X'Pert PRO X-ray diffractometer (XRD) was used to identify the phase of the powder and bulk on the model alloys. Microstructure observation and chemical composition analysis were conducted using a Hitachi-4700 scanning electron microsphere (SEM) with energy-dispersive X-ray spectroscopy (EDS). The crystal structure of different phases in the model alloys was further examined by a FEI Tecnai F20 G2 field emission gun transmission electron microscope (TEM). Vickers hardness of the model WHAs was measured with a 1 kg load and 15 s dwell time. Nanoindentation experiments were used to obtain indentation hardness and elastic modulus using the continuous stiffness measurement (CSM) method by MTS Nanoindenter XP. Compressive tests were carried out at room temperature at a strain rate of 10^{-3} S^{-1} using a universal test machine with a capacity of 100 KN.

3 Results and Discussion

3.1 Characterization of the FeCoNiCu MEA

3.1.1 XRD Analysis

Figure 1 shows the XRD spectra of the FeCoNiCu MEA powders as a function of milling time. The four elements of the binder phase can be clearly identified from the XRD spectrum of the un-milled powders. The main strong

Table 1 Particle size, purity level and supplier of the raw materials

Raw powders	Particle size (µm)	Purity level (%)	Supplier
W	1 ~ 5	> 99.5	Ultimate Materials Technology, Taiwan
Mo	3 ~ 5	> 99.9	
Co	~ 45	> 99.9	
Fe	~ 45	> 99.9	
Ni	~ 45	> 99.9	
Cu	~ 40	> 99.0	

Table 2 The chemical composition and sintering temperature of the model WHAs

Model alloy		W	Mo	Ni	Fe	Co	Cu		Sintering temperature
WMo-1250	wt%	87	3	2.48	2.35	2.49	2.68		1250 ℃
WMo-1350									1350 ℃
WMo-1450									1450 ℃
W-1450	at%	70.25	4.65	6.28	6.28	6.28	6.28		1450 ℃
	wt%	90	–	2.48	2.35	2.49	2.68		
	at%	74.33	–	6.42	6.42	6.42	6.42		

diffraction peaks are corresponding to the Cu reflections. After 4 h of milling, the Fe peak (2 theta at ~ 48°) was not observed and revealed that the Fe element dissolved into the crystal lattice of the MEA binder and formed a solid solution phase during mechanical alloying. With continued milling up to 8 h, the peaks of Cu tend to disappear or merge with the Ni peaks and form the unstable FCC transition phase. In the final stage of milling (16 h), the complete formation of a single-phase solid solution with FCC structure was achieved.

3.1.2 SEM–EDS Mapping

Figure 2 shows the SEM–EDS mapping of the sintered FeCoNiCu MEA milled for 16 h. The FeCoNiCu MEA matrix shows a light gray contrast, see the point "A", which has a uniform distribution of the elements and is close to the nominal equiatomic composition of the designed binder phase, see the table in Fig. 2. However, a small number of dark particles with a high concentration of Fe and O were observed in the microstructure, suggesting the formation of Fe-rich oxides (see the points "B" and "C" in Fig. 2a). The result also corresponds to the EDS mapping analysis, see Fig. 2b–g, indicating that the oxide particles are mainly composed of Fe and O and precipitated at the FeCoNiCu MEA matrix.

3.2 Microstructure Characterization of the Sintered Model WHAs

3.2.1 SEM/EDS

Figure 3 shows the microstructure evolution of the WMo-1450 model alloys milled for 4, 8, 12, and 20 h. It can be seen clearly that the W-Mo matrix phase appeared as bright contrast and has nearly spherical particles embedded in the FCC MEA binder phase. In the initial stage of milling (4 h), see Fig. 3a, non-uniform distribution of the W-Mo matrix and MEA binder phase was obtained and small black pores were also found in this model alloy. The microstructure tends to become more homogeneous by increasing the milling times (see Fig. 3). Besides, an enhanced densification
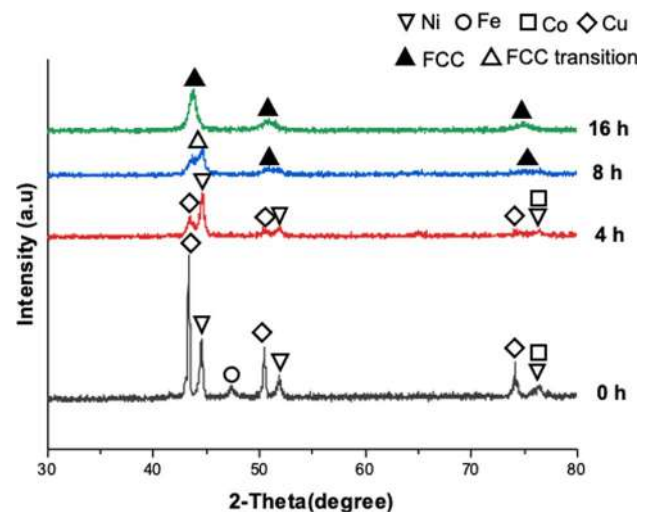

Fig. 1 XRD spectra of the FeCoNiCu MEA powders milled for 0, 4, 8, and 16 h

evolution is observed as a result of the disappearance of small pores from the binder phase during a long milling duration (see Fig. 3d). It should be pointed out that a typical structure of liquid phase sintering was apparently obtained at the model alloys for all different milling times. It suggests that Cu does not possess any mutual solubility with tungsten [22] and the immiscible system of W-Cu can therefore induce metastable liquid phase separation, promoting the liquid phase to wet the tungsten grains by a combination of solution reprecipitation and coalescence.

Figure 4 shows the SEM/EDS analysis of the sintered model alloys at different sintering temperatures. The corresponding EDS results are tabulated in Table 3. It can be seen clearly that a fined grain structure was obtained at the model alloy with a sintering temperature of 1250 °C, see Fig. 4a. The small spherical tungsten grains (~ 5 μm) were surrounded by the FCC MEA binder phases. It reveals that the FCC MEA binder phases partially melt to form a semisolid structure and thus undergo a partial liquid phase during the sintering process. Furthermore, the dark area, see the point "A" contains a high amount of Fe and O

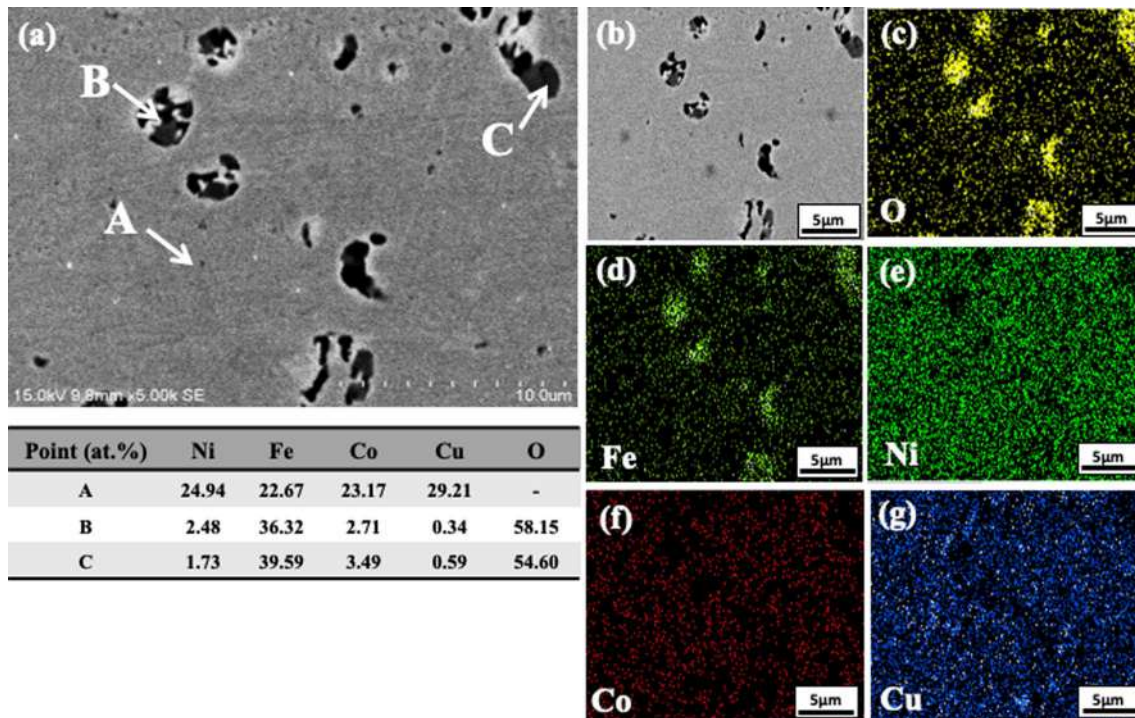| Point (at.%)	Ni	Fe	Co	Cu	O
A	24.94	22.67	23.17	29.21	-
B	2.48	36.32	2.71	0.34	58.15
C	1.73	39.59	3.49	0.59	54.60

Fig. 2 EDS mapping images of the sintered FeCoNiCu MEA milled for 16 h: **a**, **b** SEM images, **c** O map, **d** Fe map, **e** Ni map, **f** Co map, and **g** Cu map

elements, which can be associated with the formation of Fe-rich oxide in the WHA model alloys. However, in this study, the FCC MEA binder, which has a lower Fe content was detected, see the point "B". It is evident that the depletion of Fe in the binder phase promotes the Fe-rich oxide formation between the tungsten grains. On the contrary,

when the sintering temperatures were increased to 1350 and 1450 °C, a large size of spherical tungsten grains about 30 μm embedded in the MEA binder phase can be apparently demonstrated, suggesting that the formation of liquid phase sintering is dominant in the model alloys as shown in Fig. 4b–d. Besides, the FCC MEA binder

Fig. 3 SEM images of the WMo-1450 model alloy for the different milling times: **a** 4 h, **b** 8 h, **c** 12 h, and **d** 20 h
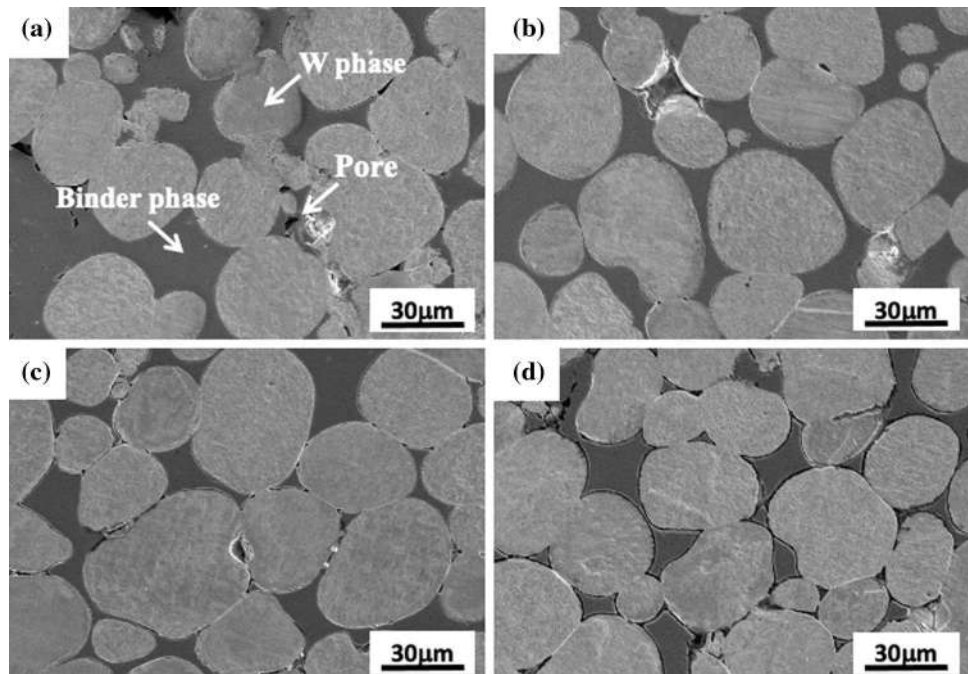
has a near equiatomic composition in the FeCoNiCu system, see the points "D" and "E". In this study, the Cu element of the MEA binder phase plays an important role in the behavior of solid/liquid phases at different sintering temperatures. The presence of Cu, which has a low melting point (1084 °C), can reduce the solid to liquid transition temperature of the FeCoNiCu MEA system. It is believed that when the sintering temperature was gradually increased, the fast diffusion rate of the liquid binder phase can increase the capillary force, which further promotes the sufficient rearrangement of tungsten grains. Moreover, Cu has a high solid solubility in the FeCoNiCu MEA binder, which can further encourage a process of solution-reprecipitation, leading to grain coarsening, dissolution of small grains, and grain rounding.

Furthermore, the model alloy without the addition of Mo sintered at 1450 °C can be seen in Fig. 4d. In this case, the microstructure coarsening was clearly observed. The result implies that the presence of Mo is a benefit for refining grain structure in tungsten heavy alloys (see Fig. 4c and d). It is also interestingly noted that as the sintering temperature increased to 1450 °C, a small gap occurred in the interface between the MEA binder phase and the tungsten matrix was observed, see the point "F" on Fig. 4d. EDS result, see Table 3, indicates that the gap received with a high concentration of oxygen, which confirmed the formation of the oxide layer. This phenomenon could be ascribed to the two combined effects. Firstly, Cu has no solubility in W and liquid phase decomposition was generated in the immiscible W-Cu system, which might result in poor wettability and bonding at the tungsten grains. Secondly, it should take into account the effect of the coefficient of thermal expansion (CTE) between the two phases. The binder phase contains a high amount of Cu element, which has a much higher thermal expansion coefficient compared to that of the tungsten matrix. Therefore, a large residual thermal stress induced by the high-temperature sintering process causes the greatest shrinkage at the grain boundaries where Fe-rich oxides were preferably formed and occupied, see the point "F". Consensually, the interfacial bonding and chemistry between the two phases were then degraded.

Fig. 4 SEM images of the model alloys milled for 20 h at different sintering temperatures: **a** WMo-1250, **b** WMo-1350, **c** WMo-1450, and **d** W-1450
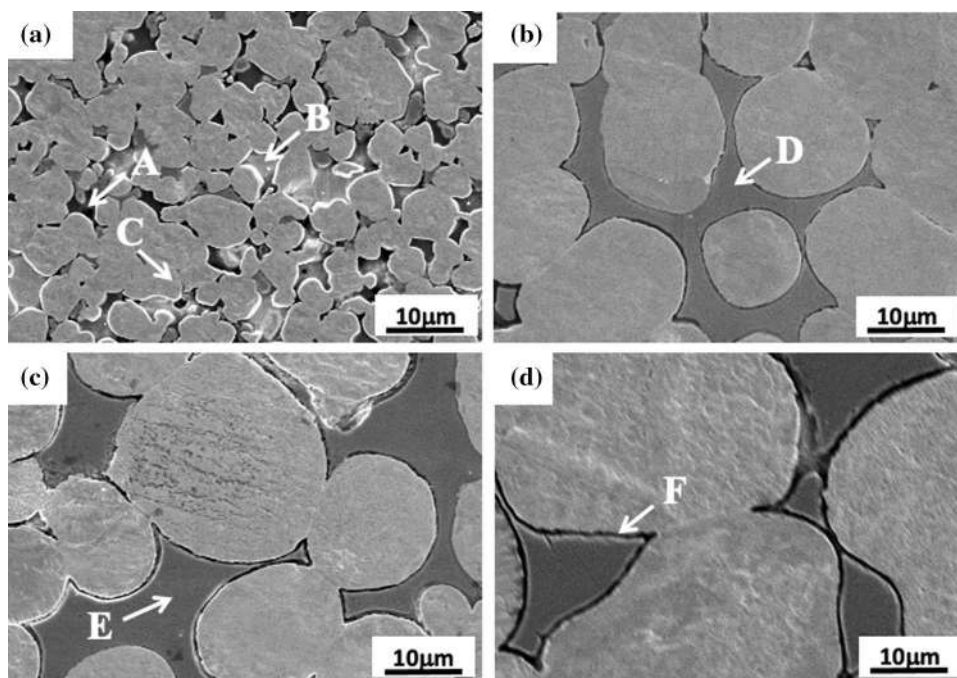

Table 3 EDS analysis of the sintered model alloys corresponding to SEM images of Fig. 4

Position (at%)	W	Mo	Fe	Co	Ni	Cu	O
Point A	43.25	1.50	11.51	8.49	4.52	2.64	28.09
Point B	10.33	0.33	6.53	27.35	30.18	25.28	–
Point C	97.20	1.31	0.68	0.05	0.23	0.82	–
Point D	10.71	1.28	19.67	22.79	24.08	21.47	–
Point E	9.97	1.09	20.03	23.27	24.92	20.72	
Point F	4.6	–	12.35	12.38	17.54	19.41	32.72

On the other hand, Fig. 5 shows the EDS mapping of the WMo-1450 model alloys. Homogeneous distribution of the tungsten grains and the binder phases is clearly observed in the SEM image, see Fig. 6a. The EDS maps, Fig. 6e–h, show the high concentration of Ni, Co, Fe, and Cu elements in the microstructure, which confirms the formation of the FCC MEA binder phase. The EDS map of W and Mo demonstrates a uniform distribution of elements, corresponding to the formation of the solid solution of the W-Mo matrix phase.

3.2.2 XRD Analysis

Figure 6 shows the XRD spectra of the milled powders for 16 h and sintered model alloys at the various temperatures of 1250, 1350, and 1450 °C. The strong reflection peaks of the tungsten and the weak peak of the FCC MEA binder phase at 2 theta of ~ 44° are observed in all the samples. The peak broadening feature is clear in the XRD pattern of the milled powders, which can be associated with high strain energy during ball milling. A large number of crystal defects generated on the milled powders can be eliminated during sintering processing, resulting in a significant recovery in the intensities of the tungsten peaks in the XRD spectra due to thermal activation facilitating the release of strain energy. The results also suggest that a higher sintering temperature leading to the formation of liquid phase sintering can promote a high degree of perfect crystalline on the material, which causes an increase in the high intensity of the peaks.

3.2.3 TEM Investigation

TEM characterization was conducted to further investigate the crystal structure of the different phases formed at the WMo-1250 model alloy, which has a fined grain structure with semisolid state sintering. Figure 7a shows the TEM image of the large grain located at the point "I", which has a high level of tungsten with a small amount of Fe, Co, Ni, and Cu. According to the selected area diffraction (SAD) pattern, see Fig. 7c, the W phase is oriented along the zone axis of $[11\bar{1}]$ with an average lattice parameter of 3.238 Å. The lattice parameter of the W phase is much large than that of pure tungsten (3.165 Å). It suggests that the presence of the Fe, Co, Ni Cu elements in the MEA binder phase can have a significant reaction with the W-Mo matrix during mechanical alloying and subsequent sintering process. A solid solution between these two phases can lead to an increase in the lattice parameter of the W phase.

On the other hand, the MEA binder phase located at point "II" has a high concentration of Fe, Co, Ni, Cu, and

W. Phase identification was performed on the SAD pattern and the phase has been indexed as an FCC structure as shown in Fig. 7d. Moreover, the twinned structure of the MEA binder phase was apparently observed in point "III". The enlarged TEM micrographs of the twinned MEA binder phase can be further seen in the dark-field image as shown in Fig. 7b. In the present study, the MEA binder phase with FCC structure has low stacking fault energy [23] and provides high work hardening, which is governed by the planar glide of dislocations. Consequently, in this case, the pre-milling of the MEA binder phase containing relatively high Cu content dominates deformation twinning during the high-energy mechanical alloying induced severe plastic deformation. It has been also proposed that twinning is more frequently observed in FCC HEAs based on 3d transition metals and plays an important role in the enhanced strain hardening rate and improved ductility [24, 25].

3.3 Mechanical Properties of the Sintered Model WHAs

3.3.1 Microhardness

Figure 8 shows the hardness values of the model alloys sintered at different temperatures as a function of milling time. The results show that the hardness of all model alloys has increased as the time of the milling increases. It can be correlated that a homogeneous microstructure accompanied by good densification was achieved after a prolonged mechanical alloying processing. Furthermore, among all model alloys, the WMo-1250 alloy exhibits the highest hardness level (419 HV). When the sintering temperatures rise to 1350 and 1450 °C, the hardness values of the model alloys significantly drop between 377 and 330HV, respectively. The results can be related to the solid-to-liquid phase transition during sintering. The higher sintering temperatures lead to the formation of liquid phase sintering, which provides rapid grain growth with an extremely coarse grain structure of the W-Mo matrix and the FCC MEA binder phase. Hoverer, the semisolid phase sintering was obtained at the model alloy with the low-temperature sintering of 1250 °C that a fined grain size and the presence of small Fe-rich oxides can promote an increase in the hardness. It is supposed that the small oxide dispersoids formed at the grain boundary could also act as a barrier against dislocation movement and grain growth [26]. Hence, it can be concluded that the sintering temperatures can have a significant impact on the sintering behavior of the model alloys changed from solid to liquid phase sintering, which corresponds to the decrease in hardness. In addition, the Mo-free model alloy (W-1450) has a low hardness value of 330HV, which is a reduction
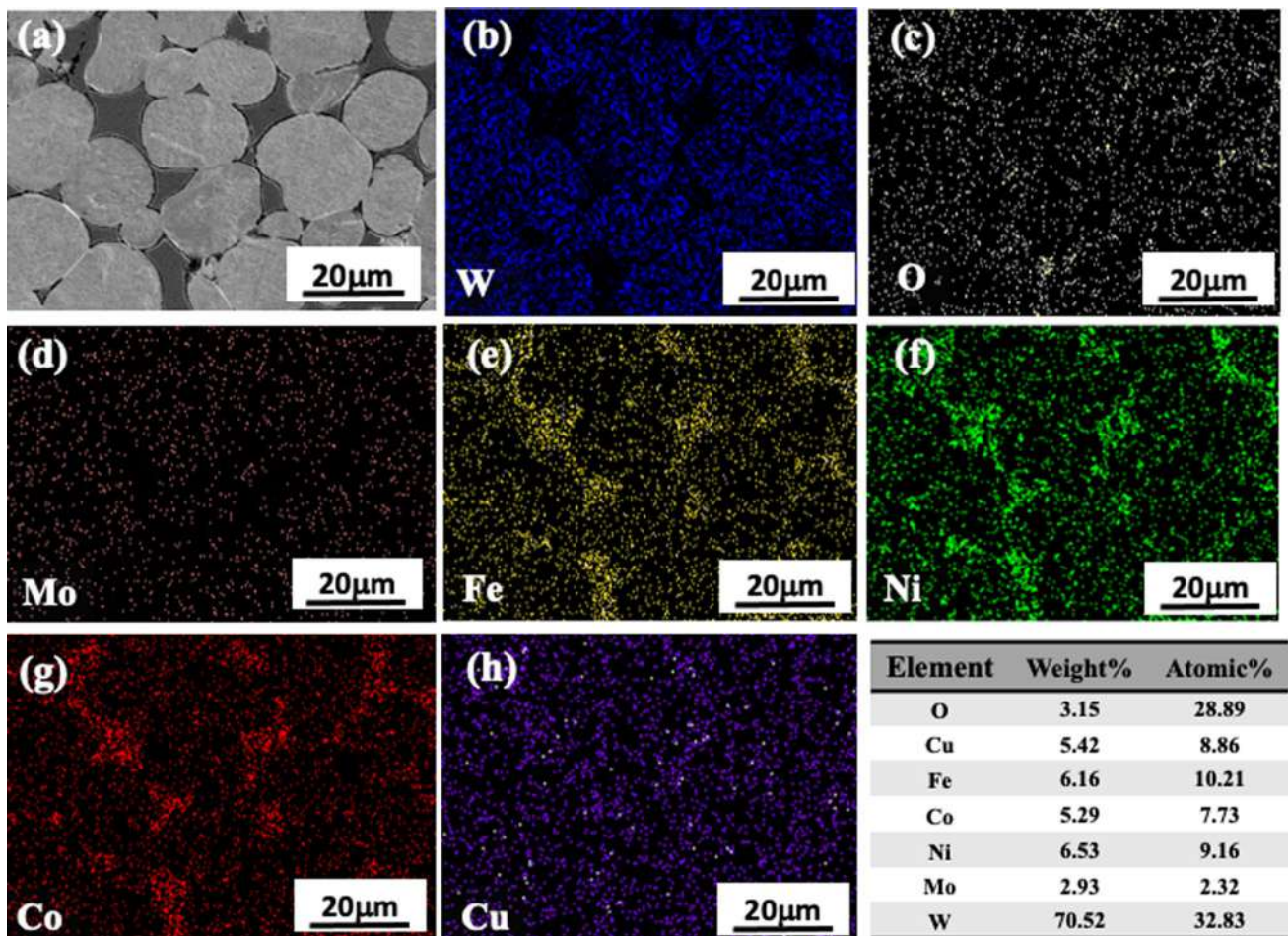
Element	Weight%	Atomic%
O	3.15	28.89
Cu	5.42	8.86
Fe	6.16	10.21
Co	5.29	7.73
Ni	6.53	9.16
Mo	2.93	2.32
W	70.52	32.83

Fig. 5 EDS mapping images of the WMo-1450 model alloy: **a** SEM image, **b** W map, **c** O map, **d** Mo map, **e** Fe map, **f** Ni map, **g** Co map, and **h** Cu map
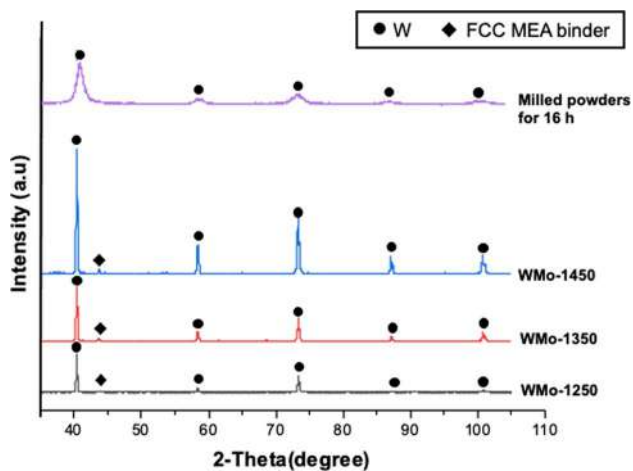

Fig. 6 XRD spectra of the model alloys milled for 20 h at different sintering temperatures

of 10% in hardness compared to the Mo-containing sample (WMo-1450). It suggests that the addition of Mo in the model alloy can form a solid solution of the W-Mo matrix and also refine the microstructure, improving the mechanical properties of materials.

3.3.2 Nanoindentation

In order to examine the mechanical properties of individual phases, nanoindentation tests were further applied for the WMo-1450 sample, which has a very coarse grain structure of about 30 μm. The nanoindentation hardness and elastic modulus of the W-Mo matrix and the FCC MEA binder phase of the model alloy were obtained as shown in Fig. 9. The W-Mo matrix has a high hardness of 5.34 GPa and an elastic modulus of 334.77 GPa, see Fig. 9a. However, the MEA binder phase possesses a low value of hardness and elastic modulus (2.31 and 155.17 GPa) as shown in Fig. 9b. It should be noted that the indentation is not perfectly
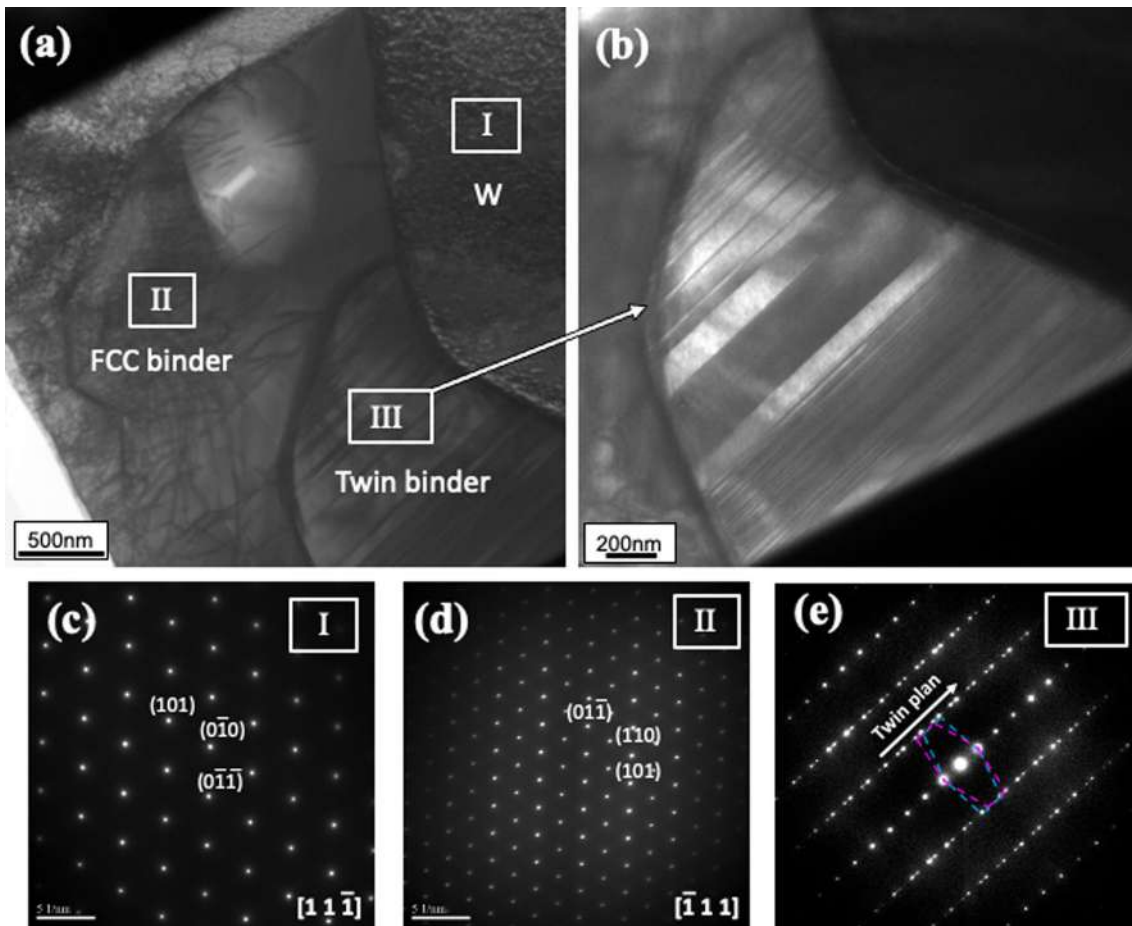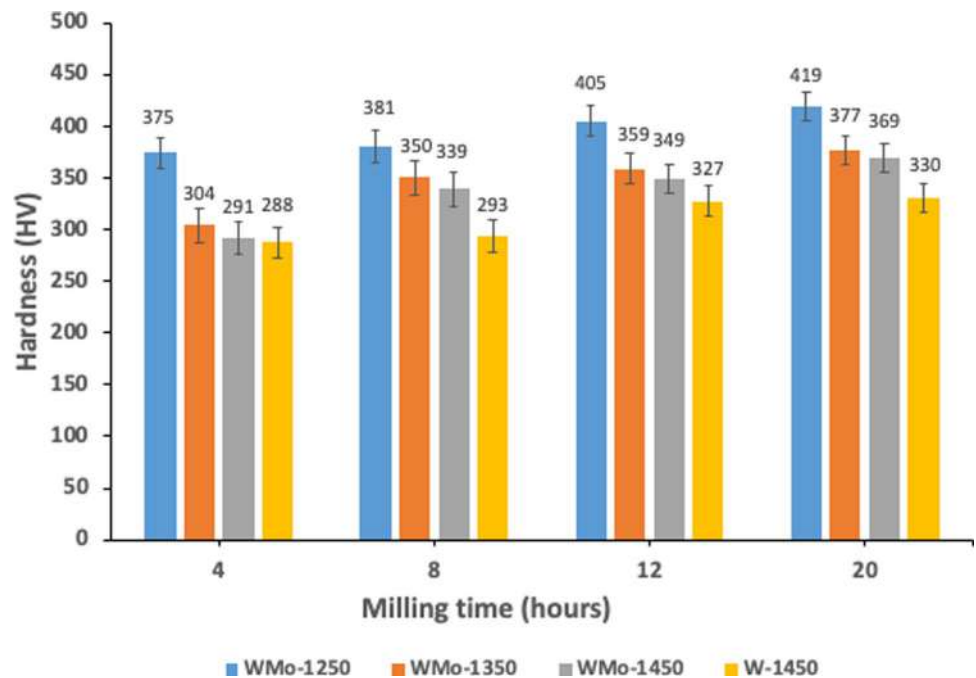
Fig. 7 TEM investigations of the WMo-1250 model alloy: **a** TEM image, **b** Dark-field image of the MEA binder phase with twinned structure, and **c**, **d**, **e** The SAD patterns of the points "I", "II" and "III" in Fig. 7a

Fig. 8 The microhardness of the model alloys at the different milling durations and sintering temperatures

located at the MEA binder phase and therefore the result can be strongly influenced by the surrounding W-Mo matrix.

The nanoindentation test was also performed on the interface of the MEA binder and W-Mo matrix, see Fig. 9c. The result indicates that a medium value of hardness and elastic modulus was obtained (3.58 and 211.05GPa) in the interface area of the model alloy. It reveals that the binder phases behave with a high degree of ductile nature, which is important for enhancing the ductility of the brittle W-Mo matrix.

3.3.3 Compression Testing

The compression tests were further performed on the WMo-1250 and WMo-1450 model alloys, which have a large difference in hardness and microstructure characteristics. The engineering stress–strain curves of the specimens under uniaxial compression testing are plotted in Fig. 10. In the WMo-1250 sample, the stress is linearly related to the strain during elastic deformation and compressive yield strength

of ~ 900 MPa was determined using 0.2% offset method. After large plastic deformation followed by the occurrence of elastic deformation, the specimen has ultimate compressive stress (UCS) of 2080 MPa and compressive failure strain of 42%. The results seem to be higher than that of the use of a conventional binder phase in WHAs in most cases [28–29] and very competitive with LPBF-printed W–Ni-Fe alloy, which has a considerably high compressive strength of 2638 MPa and a strain of 46% [30]. In the present work, the good combination of compressive strength and ductility can be attributed to the fined grain structure related to the formation of semisolid phase sintering and the high amount of Cu in the FCC MEA binder phase, which is more ductile in nature, increasing the plasticity of WHAs. It should be pointed out that deformation twins were obtained in the FCC MEA binder phase, which can increase work hardening and improve the plasticity as reported in FCC-based HEAs [31, 32]. However, when the model alloy is sintered at 1450 °C, the compressive strength (630 MPa) and fracture strain
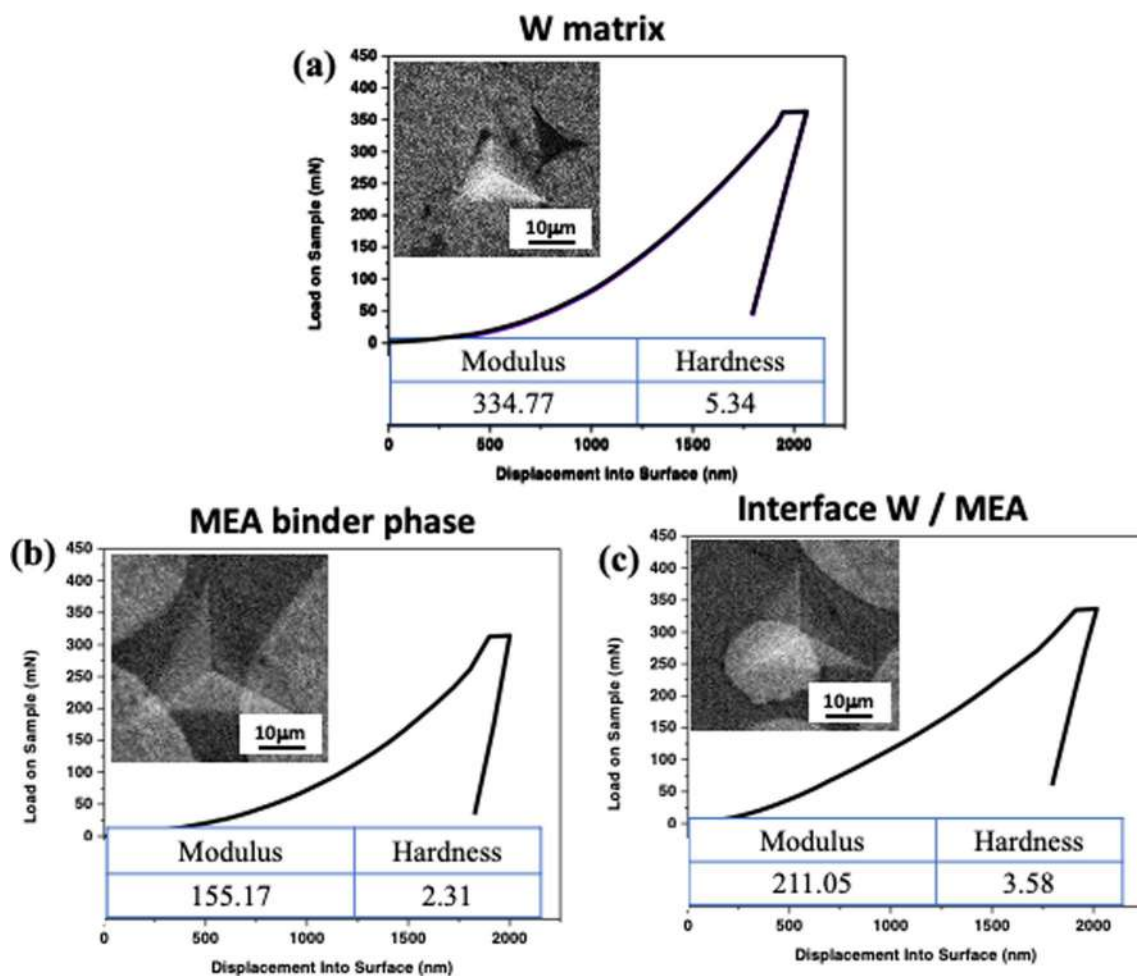

Fig. 9 Nanoindentation tests of the model alloys sintered at 1450 °C: **a** Tungsten matrix, **b** MEA binder phase, **c** Interface between the binder and matrix
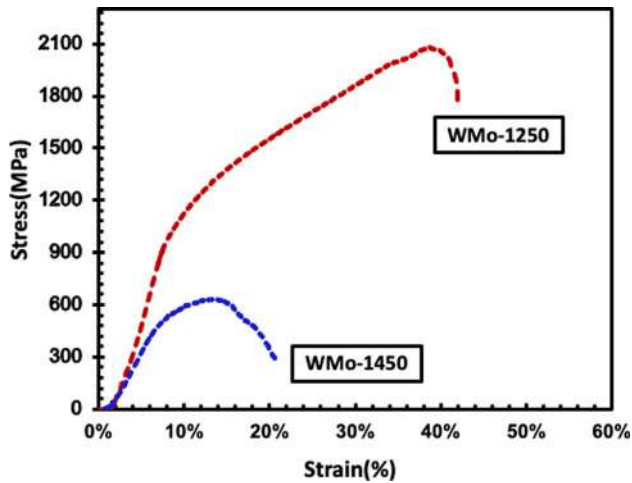
Fig. 10 Compressive engineering stress–strain curves of the WMo-1250 and WMo-1450 model alloys

Table 4 Theoretical density and relative density of the model alloys

Model alloys	Theoretical density (g/cm^3)	Relative density (%)
WMo-1250	16.758	98.48
WMo-1350	16.758	92.88
WMo-1450	16.758	89.09
W-1450	17.149	88.73

(21%) can be considerably reduced due to the large grain structures developed during liquid phase sintering and the poor interfacial bonding strength between the binder and W-Mo matrix. Besides, the relative density of the W-Mo model alloys was measured by Archimedes' principle, see Table 4. A high relative density of 98.48% was obtained in the WMo-1250 sample, which has a high hardness, compressive strength, and compressive strain. However, a drop in relative density to 89.09% was received in the WMo-1450 sample, which corresponds to the degradation of mechanical

properties due to material densification and the effect of oxide layer formation at grain boundaries.

Figure 11 shows the fracture surface of the failed compression samples. The results revealed that very fine fracture surface features were observed in the WMo-1250 alloy as shown in Fig. 11a and b. The dark tungsten grains are surrounded by the bright MEA binder phases and indicate that intergranular fracture is the dominant failure mode. Conversely, the ultra-large fracture surface morphology was obtained at the sample sintered at 1450 °C as shown in Fig. 11c and d. In this case, W–W boundary was the weakest interface in the alloy, and thus W-W interface failure with the W cleavage facet becomes the dominant fracture mode. Transgranular fracture and tearing ridge were also visible from the fracture surface. It should be noted that Fe-rich oxide layers can form along the grain boundary, which causes delamination between the two phases, leading to a deterioration in the mechanical properties of the model WHAs.

Fig. 11 Fracture surfaces of **a**, **b** the WMo-1250 and **c**, **d** WMo-1450 model alloys after compression tests
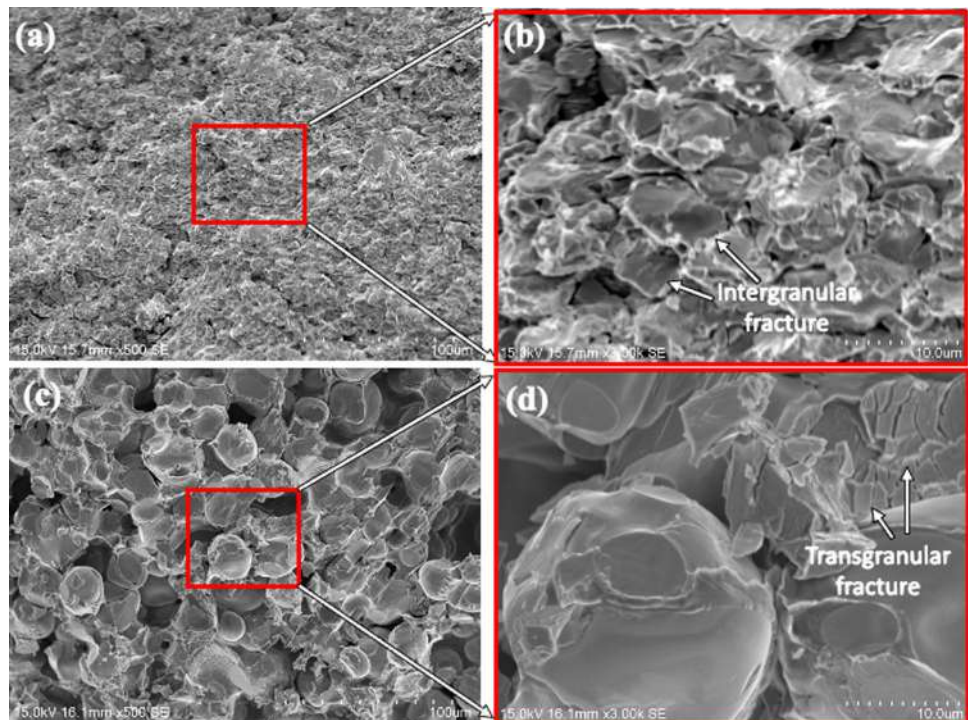
4 Conclusions

FeCoNiCu MEAs serve as a binder phase for tungsten heavy alloys that were synthesized by mechanical alloying. The role of Cu in the MEA binder phase and the effect of sintering temperatures on microstructure characteristics and mechanical properties of the WHA model alloys were investigated. The results demonstrate that the formation of a single-phase solid solution with FCC structure was achieved in the FeCoNiCu MEA system after 16 h of milling. However, the Fe-rich oxide particles were formed and dispersed in the FeCoNiCu MEA after sintering. At the low sintering temperature of 1250 °C, the small spherical tungsten grains (~5 μm) embedded in the MEA binder phases were obtained. In this case, the FCC MEA binder phases partially melt to form a semisolid structure and produce a refined microstructure. Thus, an excellent combination of high strength and good ductility was achieved in the model alloy. However, at the higher sintering temperatures (1350 and 1450 °C), a large size of spherical tungsten grains (~30 μm) can be generated, which corresponds to the formation of the liquid phase sintering dominating in the model alloys. It should be pointed out that the increased sintering temperatures can cause the formation of Fe-rich oxides along the grain boundaries, thereby resulting in significant degradation of mechanical properties.

Declarations

References

1. A. Arora, V.G. Rao, Mater. Technol. **19**, 210 (2004). https://doi.org/10.1080/10667857.2004.11753087
2. O. Dinçer, M.K. Pehlivanoǧlu, N.K. Çalis̨kan, I. Karakaya, A. Kalkanli, Int. J. Refract. Met. Hard Mater. **50**, 106 (2015). https://doi.org/10.1016/j.ijrmhm.2014.12.009
3. Y. Sahin, J. Powder Technol. **2014**, 764306 (2014). https://doi.org/10.1155/2014/764306
4. K.H. Lee, S.I. Cha, H.J. Ryu, S.H. Hong, Mater. Sci. Eng. A **458**, 323 (2007). https://doi.org/10.1016/j.msea.2007.01.118
5. A. Upadhyaya, S.K. Tiwari, P. Mishra, Scripta Mater. **56**, 5 (2007). https://doi.org/10.1016/j.scriptamat.2006.09.010
6. A. Bose, R.M. German, Metall. Trans. A **19**, 3100 (1988). https://doi.org/10.1007/BF02647738
7. P.B. Kemp, R.M. German, Metall. Mater. Trans. A **26**, 2187 (1995). https://doi.org/10.1007/BF02670690
8. C.L. Chen, Sutrisna, Metals **9**, 111 (2019). https://doi.org/10.3390/met9020111
9. Z.A. Hamid, S.F. Moustafa, W.M. Daoush, F.A. Mouez, M. Hassan, Open J. Appl. Sci. **3**, 15 (2013). https://doi.org/10.4236/ojapps.2013.31003
10. H.J. Ryu, S.H. Hong, Mater. Sci. Eng. A **363**, 179 (2003). https://doi.org/10.1016/S0921-5093(03)00641-5
11. Y.B. Zhu, Y. Wang, X.Y. Zhang, G.W. Qin, Int. J. Refract. Met. Hard Mater. **25**, 275 (2007). https://doi.org/10.1016/j.ijrmhm.2006.08.003
12. C.-L. Chen, S.-H. Ma, J. Alloy. Compd. **731**, 78 (2018). https://doi.org/10.1016/j.jallcom.2017.09.125
13. A.R. Annamalai, J.K. Chaurasia, M. Srikanth, D.K. Agrawal, C.-P. Jen, Mater. Res. Express **7**, 126503 (2020). https://doi.org/10.1088/2053-1591/abccf7
14. J.W. Yeh, S.K. Chen, S.J. Lin, J.Y. Gan, T.S. Chin, T.T. Shun, C.H. Tsau, S.Y. Chang, Adv. Eng. Mater. **6**, 299 (2004). https://doi.org/10.1002/adem.200300567
15. Y. Zhang, T.T. Zuo, Z. Tang, M.C. Gao, K.A. Dahmen, P.K. Liaw, Z.P. Lu, Prog. Mater Sci. **61**, 1 (2014). https://doi.org/10.1016/j.pmatsci.2013.10.001
16. H. Ma, Y. Shao, C.H. Shek, Int. J. Refract. Metal Hard Mater. **98**, 105572 (2021). https://doi.org/10.1016/j.ijrmhm.2021.105572
17. P.V. Satyanarayana, R. Sokkalingam, P.K. Jena, K. Sivaprasad, K.G. Prashanth, Metals **9**, 992 (2019). https://doi.org/10.3390/met9090992
18. C.-L. Chen, Sutrisna, Intermetallics **138**, 107320 (2021). https://doi.org/10.1016/j.intermet.2021.107320
19. A. Panigrahi, T.S. Acharya, P. Sengupta, D. Kumar, L. Sarangi, N. Kumar, D. Debasish, S. Suwas, S. Basu, M. Debata, Mater. Sci. Eng. A **832**, 142451 (2022). https://doi.org/10.1016/j.msea.2021.142451
20. J.I. Hyun, K.H. Kong, K.C. Kim, W.T. Kim, D.H. Kim, Appl. Microsc. **45**, 9 (2015). https://doi.org/10.9729/am.2015.45.1.9
21. X. Sun, H. Zhu, J. Li, J. Huang, Z. Xie, Mater. Chem. Phys. **220**, 449 (2018). https://doi.org/10.1016/j.matchemphys.2018.09.022
22. Y. Li, J. Zhang, G. Luo, Y. Sun, Q. Shen, L. Zhang, J. Mater. Res. Technol. **10**, 121 (2021). https://doi.org/10.1016/j.jmrt.2020.12.013
23. F. Otto, A. Dlouhý, C. Somsen, H. Bei, G. Eggeler, E.P. George, Acta Mater. **61**, 5743 (2013). https://doi.org/10.1016/j.actamat.2013.06.018
24. R.E. Kubilay, W.A. Curtin, Acta Mater. **216**, 117119 (2021). https://doi.org/10.1016/j.actamat.2021.117119
25. W. Wu, M. Song, S. Ni, J. Wang, Y. Liu, B. Liu, X. Liao, Sci. Rep. **7**, 46720 (2017). https://doi.org/10.1038/srep46720
26. C. Suryanarayana, E. Ivanov, V.V. Boldyrev, Mater. Sci. Eng. **304–306**, 151 (2001). https://doi.org/10.1016/S0921-5093(00)01465-9
27. Y. Yu, C. Ren, W. Zhang, Int. J. Refract. Met. Hard Mater. **76**, 149 (2018). https://doi.org/10.1016/j.ijrmhm.2018.06.006
28. K. Hu, X. Li, M. Guan, S.G. Qu, X.Y. Yang, J.X. Zhang, Int. J. Refract. Met. Hard Mater. **58**, 117 (2016). https://doi.org/10.1016/j.ijrmhm.2016.04.010
29. F. Xiao, T. Barriere, G. Cheng, Q. Miao, S. Zuo, S. Wei, L. Xu, J. Alloy. Compd. **878**, 160335 (2021). https://doi.org/10.1016/j.jallcom.2021.160335
30. M. Guo, K. Liu, J. Sun, D. Gu, Mater. Sci. Eng A **843**, 143096 (2022). https://doi.org/10.1016/j.msea.2022.143096
31. R.E. Kubilay, W.A. Curtin, Acta Mater. **216**, 117119 (2021). https://doi.org/10.1016/j.actamat.2021.117119
32. S.-H. Joo, H. Kato, M.J. Jang, J. Moon, C.W. Tsai, J.W. Yeh, H.S. Kim, Mater. Sci. Eng. A **689**, 122 (2017). https://doi.org/10.1016/j.msea.2017.02.043